THE JOURNAL OF PHYSICAL CHEMISTRY A

ARTICLE

pubs.acs.org/JPCA

Solid State and Solution Nitrate Photochemistry: Photochemical Evolution of the Solid State Lattice

Sanford A. Asher,* David D. Tuschel, Todd A. Vargson, Luling Wang, and Steven J. Geib

Department of Chemistry, University of Pittsburgh, Pittsburgh Pennsylvania 15260, United States

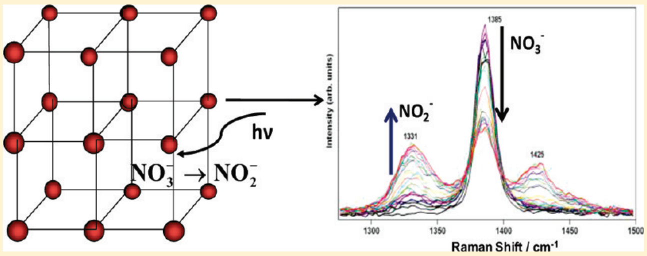

ABSTRACT: We examined the deep UV 229 nm photochemistry of $NaNO_3$ in solution and in the solid state. In aqueous solution excitation within the deep UV NO_3^- strong $\pi \rightarrow \pi^*$ transition causes the photochemical reaction $NO_3^- \rightarrow NO_2^- + O\cdot$. We used UV resonance Raman spectroscopy to examine the photon dose dependence of the NO_2^- band intensities and measure a photochemical quantum yield of 0.04 at pH 6.5. We also examined the response of solid $NaNO_3$ samples to 229 nm excitation and also observe formation of NO_2^-. The quantum yield is much smaller at $\sim 10^{-8}$. The solid state $NaNO_3$ photochemistry phenomena appear complex by showing a significant dependence on the UV excitation flux *and* dose. At low flux/dose conditions NO_2^- resonance Raman bands appear, accompanied by perturbed NO_3^- bands, indicating stress in the $NaNO_3$ lattice. Higher flux/dose conditions show less lattice perturbation but SEM shows surface eruptions that alleviate the stress induced by the photochemistry. Higher flux/dose measurements cause cratering and destruction of the $NaNO_3$ surface as the surface layers are converted to NO_2^-. Modest laser excitation UV beams excavate surface layers in the solid $NaNO_3$ samples. At the lowest incident fluxes a pressure buildup competes with effusion to reach a steady state giving rise to perturbed NO_3^- bands. Increased fluxes result in pressures that cause the sample to erupt, relieving the pressure.

INTRODUCTION

$NaNO_3$ is utilized in many chemical and industrial processes, and also utilized as an energetic material in explosives. It is important to understand the factors that enable $NaNO_3$ to function as an explosive and to develop methods to easily, remotely detect it.[1−3] In the work here we utilize deep UV resonance Raman spectroscopy (UVRRS) to probe the nature of the $NaNO_3$ electronic excited states and their complex photochemistry.[4,5] We find strong RR enhancement of the NO_3^- stretching fundamentals, as well as overtones, indicating that the excited state is displaced relative to the ground state.[6−10] The large deep UV Raman cross sections and the large number of intense overtones and combinations indicate that $NaNO_3$ can be spectroscopically detected easily with deep UV excitation.[11−13] UVRR may prove a useful technique for stand off monitoring of NO_3^- species.

We find that the displaced NO_3^- excited state correlates with a facile NO_3^- photochemistry in aqueous solution with 229 nm light;[14−22] we measure a quantum yield, $\varphi \approx 0.04$ for the photolysis: $NO_3^- \rightarrow NO_2^- + O\cdot$. We demonstrate that this photochemistry also occurs in the solid state, but that the lattice constraints dramatically decrease the quantum yield. This monophotonic photochemistry at individual lattice sites perturb NO_3^- molecules at adjacent lattice sites, shifting the NO_3^- Raman bands. The perturbations of the NO_3^- lattice sites depend upon not only the photon dose but also on the laser flux. Higher doses and fluxes give rise to photochemistry that degrade and excavate the solid $NaNO_3$ surfaces.

We carefully examined the evolution of the lattice as the photochemistry progressed. We also examined the photochemical quantum yield for photolysis in the solid state of $NaNO_3$ to examine the dependence of the activation barriers for photochemistry on the lattice geometry.

The work here also characterizes the evolution of the deep UV Raman spectra of $NaNO_3$ with deep UV excitation. This information will prove valuable for defining the time and flux varying Raman signature of these types of compounds upon deep UV excitation, that might be used, for example, for standoff detection. These studies also examine the dependence of photochemistry on solid state molecular constraints.

EXPERIMENTAL SECTION

UV Raman measurements were obtained by using the instrumentation previously described.[23,24] Briefly, excitation utilized a Coherent Industries Innova 300 FreD frequency doubled Ar$^+$ laser to generate CW 229 nm excitation. We utilized a modified Spex Triplemate spectrograph and a Princeton Instruments CCD camera (Spec-10 System, Model 735−0001). Aqueous solution $NaNO_3$ and $NaNO_2$ molar absorptivities were obtained from Ianoul et al.[25]

SEM measurements were obtained by using a Phillips FEG XL-30 FESEM. The $NaNO_3$ solid sample was translated across the 20 μm diameter spot size 229 nm laser beam at a rate of ~0.25 cm/min during which the UV Raman spectra were measured.

Received: January 14, 2011
Revised: February 17, 2011
Published: April 04, 2011

dx.doi.org/10.1021/jp200406q | *J. Phys. Chem. A* 2011, 115, 4279–4287

The sample was then sputter coated with Pd for subsequent SEM studies.

X-ray Powder Diffraction. X-ray powder diffraction patterns were collected using a Bruker AXS D8 Discover powder diffractometer at 40 kV, 40 mA for Cu Kα, (λ = 1.5406 Å) radiation with a scan speed of 0.20 s/step and a step size of 0.02018°. Samples were prepared by finely grinding the sample with a mortar and pestle and then evenly dispersing the powder on a vaseline-coated glass slide. The data were analyzed for *d*-spacings by using the Bruker Powder Analysis Software package EVA program.

We compared our powder diffraction data to that of the Inorganic Crystal Structure database and the American Mineralogist Database to search for comparable literature powder patterns. The $NaNO_3$ directly obtained from JT Baker (Analyzed Reagent) showed a very good correlation with $NaNO_3$ crystallized in the trigonal R $-$3c space group ($a = b = 5.077$ Å, $c = 16.82$ Å)[26−28] with the five largest peaks at *d*-spacings of 3.07, 2.85, 2.32 1.92, and 1.90 Å.

We studied a solid sample that we prepared to be fully dense in order to ensure high thermal conductivity. These solid samples were prepared by melting an anhydrous crystalline sample of $NaNO_3$ (J. T. Baker Analyzed Reagent) in a oven (T_{max}= 360 °C). The melted sample was allowed to cool over a period of 16 h. The $NaNO_3$ sample cooled from the melt gave some powder diffraction peaks identical to those above, but the diffraction from the two samples clearly differ. A search of the database found another $NaNO_3$ polymorph that crystallizes in the trigonal $R3\bar{m}$ space group ($a = b = 5.084$ Å, $c = 8.175$ Å)[26] whose diffraction closely matches the melt sample (largest *d*-spacings at 3.88, 3.00, 2.73, 1.86, and 1.85 Å. The differences observed between the relative diffraction intensities for the melt compared to the literature compound we attribute to a somewhat lower melt sample crystallinity.

The $R3\bar{c}$ structure contains alternating layers of Na^+ and NO_3^- groups, with NO_3^- anions in alternating layers rotated 60° relative to one another. Paul and Pryor[26] report a phase transition to a $R3\bar{m}$ structure at 275° where the *c*-axis spacing is halved and two NO_3^- orientations are disordered (each N atom has 6 half-occupancy O atoms coordinated).

Solution UV Raman Measurements. A 1.5 mL aqueous solution containing 0.0387 mg/mL $NaNO_3$ was placed in a 1 cm path length fused silica cuvette that was continuously stirred by using a small magnetic stir bar. The sample was excited in an almost backscattering geometry (150°) by a 229 nm ~0.45 mW CW laser beam (at the cuvette surface). The stirred samples were illuminated for extended time periods and UV Raman spectra were measured during short time accumulations during and after sample illumination periods. The 20 μm beam waist (measured in air) was focused just inside the cuvette window.

Solid UV Raman Measurements. We prepared fully dense samples of $NaNO_3$ to avoid any uncertainty concerning thermal conductivity in our solid samples, such as that which would occur for small packed crystallites where thermal conductivity could be inhibited by the presence of air pockets between packed crystals.

We heated the reagent $NaNO_3$ powder in an oven to 360 °C where it melted. We allowed it to slowly cool over 16 h to room temperature. During cooling it formed a monolith consisting of multiple grains. The stationary solid $NaNO_3$ measurements were obtained from static samples by attaching thin ~0.2 cm^2 pieces onto a sample holder in the spectrometer with double stick tape. The laser beam was focused onto the sample surfaces by using a 10 cm focal length fused silica lens. The focal spot was measured at the sample to have a 1/e diameter of 20 μm.

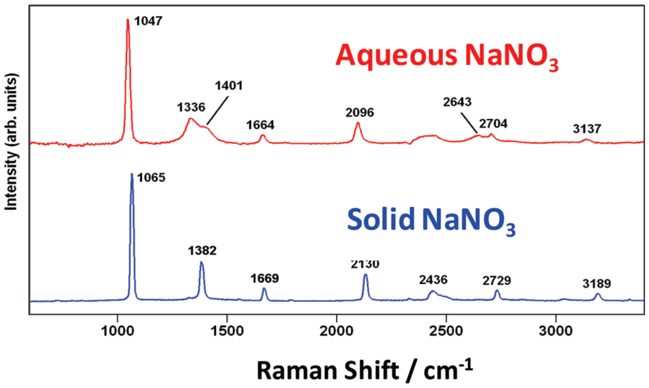

Figure 1. Comparison of 229 UVRR spectrum of an aqueous solution of $NaNO_3$ to that of a spinning solid sample.

We decreased the *average* laser flux onto the solid samples by utilizing a spinning cell where flat solid sample pieces were wedged into circular grooves in the flat surface of a cylindrical spinning metal sample holder. To avoid movements of the beam on the sample as we varied the illumination power we altered the laser power by swapping metallic film neutral density filters in the beam.

RESULTS AND DISCUSSION

Figure 1 shows the 229 nm aqueous solution and solid state UVRR of $NaNO_3$. This excitation occurs within the very strong 205 nm lowest energy allowed $\pi \rightarrow \pi^*$ transition.[4,5,11−13,25] There is also a lower energy very weak absorption centered around 310 nm.

The solution and solid state UVRR spectra are strikingly similar showing dominating enhancements of the NO_3^- $\nu 1$ symmetric stretching vibrations at ~1047 and 1065 cm^{-1} for the solution and solid state samples, respectively. The first and second overtones of $\nu 1$ also show significant intensities. The NO_3 $\nu 3$ antisymmetric stretch between 1336 and 1401 cm^{-1} shows significant intensities, and is interestingly split in water. The first overtones are also clearly observed for this vibration.

The out-of-phase $\nu 2$ 830 cm^{-1} vibration is not evident in either the solution or solid state spectrum, but its overtones are clearly evident as bands at ~1666 cm^{-1}. Other combinations and overtones are also clearly present.

We showed previously that the strong 205 nm NO_3^- $\pi \rightarrow \pi^*$ transition dominates the resonance Raman enhancement of the solution spectra.[25] The similar aqueous solution and solid spectra clearly indicate very similar resonant transitions. The strong resonance enhancement and the overtone scattering clearly indicates that the resonant excited state is displaced along the N−O bonds. Indeed, Waterland and Myers[11,12] extensively examined resonance enhancement of KNO_3 in aqueous solution and observed essentially identical spectra. They analyzed the excitation profiles in detail using the time dependent wave packet formalism and concluded that the N−O bond lengths were expanded by ~7 pm in the excited state. Gaff and co-workers have developed a method for calculating resonance Raman cross sections through ab initio calculations based upon the optimization of ground and excited state geometries. For the case of the nitrate anion, they found a difference of ~8 pm between the ground and excited state bond lengths.[5] We are presently

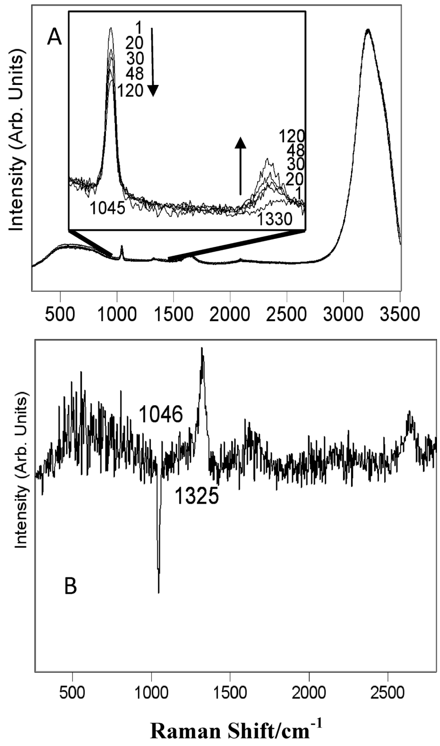

Figure 2. (A) 229 UV Raman spectra of a 0.0387 mg/mL aqueous solution of $NaNO_3$ as a function of exposure time. (B) difference spectrum between 48 min illumination time and the initial spectrum.

analyzing the overtone patterns to get further information on the excited state displacement.

Interestingly, we see significant photochemistry for the solution and solid phase samples of $NaNO_3$ as shown below. However, the quantum yields dramatically differ between the two phases. It is large for the solution phase and very small for the solid state. This suggests that the solid state photochemical reaction coordinate involves additional constraints that limit the quantum yield from that in water.

Solution Phase Photochemistry. Figure 2A examines the illumination time dependence of the 229 nm Raman spectra of an aqueous $NaNO_3$ solution. As noted by Narayanswamy[29] UV illumination of nitrate salts results in the formation of nitrites and molecular oxygen: $NO_3^- + h\nu \rightarrow NO_2^- + O\cdot$. The resulting photolysis decreases the NO_3^- band intensity at 1045 cm^{-1} and generates an increasing intensity for the broad NO_2^- peak at 1330 cm^{-1}. Figure 2B shows the difference spectrum between the 48 min illumination and the original aqueous $NaNO_3$ solution. The difference spectrum clearly shows a trough at 1046 cm^{-1} resulting from NO_3^- loss and a peak at 1325 cm^{-1} showing NO_2^- formation.[25]

For low conversion conditions the photolysis quantum yield can be determined from:

$$\phi \sim \frac{\left[\left(\dfrac{I_{NO_2^-}}{I_{NO_3^-}}\right)\right]\left(\dfrac{\sigma_{NO_3^-}}{\sigma_{NO_2^-}}\right)\cdot C_{NO_3^-}\cdot V\cdot N_{AV}}{\displaystyle\int_0^t photons(t)\cdot dt}$$

The relative number of nitrite molecules produced was determined from the relative peak intensities normalized to the relative Raman cross section values which we measured to be ($\sigma_{NO3}/\sigma_{NO2} = 0.65$).[25] The illumination photon dose was determined from the measured intensity of the laser and corrected for reflection losses from the cuvette surfaces using the Fresnel equation with an interior refractive index of water. V is the sample volume and N_{AV} is the Avogadro's number. We find $\varphi = 0.04$ for the aqueous solution quantum yield.

Solid Phase Photochemistry. The photochemical response of solid $NaNO_3$ samples to 229 nm excitation is highly dependent on both the light flux (power/area) and dose (photons/area). Thus, we will discuss the laser illumination response phenomena starting from low flux and dose conditions. We simultaneously achieved low excitation flux conditions and high UVRR S/N ratios by spinning the solid $NaNO_3$ samples. The lowest flux illuminated solid samples were packed within a 1.5 cm diameter, ~2 mm wide groove in a spinning cell. The solid sample fragments were packed into the groove such that the flat fragment sample surfaces were approximately at the same height from the groove surface bottom. The spinning cell was mounted with its axis of rotation parallel to the optical axis of the collection lens and the cell was spun at >600 rpm. The 229 nm laser excitation beam excited the spinning sample approximately in a backscattering geometry with the laser beam focused to a ~20 μm diameter spot. The CW incident, 229 nm, ~0.5 mW beam resulted in a flux of ~48 mW/cm^2 within the illuminated sample annulus.

Figure 3A compares the UVRR of the illuminated spinning sample of solid $NaNO_3$ to a spinning solid sample of $NaNO_2$. At the earliest times the $NaNO_3$ sample shows the NO_3^- $\nu1$ symmetric stretching band at 1068 cm^{-1}, the $\nu3$ antisymmetric stretching band at 1385 cm^{-1}, the overtone of the forbidden $\nu2$ band at 1670 cm^{-1}, the first overtone of the $\nu1$ band at 2133 cm^{-1}, the combination of the $\nu1$ and $\nu3$ bands at 2440 cm^{-1}, the first overtone of the $\nu3$ band at 2733 cm^{-1}, and the third overtone of the $\nu1$ band at 3192 cm^{-1}.

As illumination progresses, we observe photolysis of NO_3^- to NO_2^- as evident in formation of the 1331 and 2654 cm^{-1} peaks that derive from the NO_2^- $\nu1$ stretch and its overtone band that dominates the spectrum of $NaNO_2$. The intensity of the NO_2^- peaks increase as the illumination times increase as evident in Figure 3B that expands the $\nu3$ band region. We are, as yet, uncertain of the origin of the growing 1766 cm^{-1} peak.

In addition to the increasing intensity of the NO_2^- bands, we see an upshift in the frequency of the $\nu1$ symmetric stretching band from 1068 to 1077 cm^{-1} (Figure 3C). Accompanying this NO_3^- band upshift with increasing illumination time, there is a loss of intensity in the $\nu3$ antisymmetric stretching band at 1385 cm^{-1} accompanied by the formation of a new band at 1425 cm^{-1}. This band is assigned to an upshifted perturbed $\nu3$ antisymmetric stretching band; the frequency sensitivity of the $\nu3$ band is ~4 times that of the $\nu1$ band.[3,4,30−33]

This NO_3^- band upshift obviously results from perturbations of the $NaNO_3$ lattice due to the photochemical formation of NO_2^- and $O\cdot$. One possibility (consistent with results below) is that pressure in the lattice increases with photolysis and that the stress induces frequency upshifts due to mechanical compression of the NO_3^- groups (see below).

This spectral response to laser illumination does not result from laser heating. As shown below the high heat conductivity of fully dense solid $NaNO_3$ sample results in a negligible sample temperature increase of <5 °C from our 229 nm excitation beam.

Figure 4 shows the time dependence (in units of dose) of the increasing intensity of the photochemically produced NO_2^-

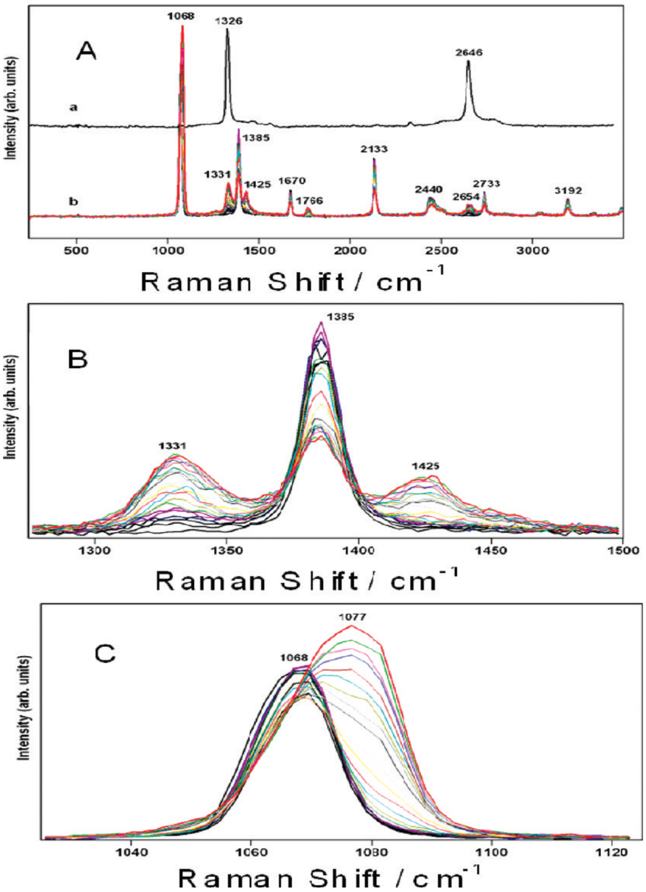

Figure 3. (A) Comparison of 229 nm UVRR spectra of (a) spinning sample of solid $NaNO_2$ to (b) that of a spinning sample of solid $NaNO_3$ as a function of illumination time. The spectra were 1 min accumulation times. The first seven spectra were spaced by 5 min intervals, the next three by 15 min intervals and the remainder by 30 min intervals. Incident flux is 0.45 mW power into a 20 μm spot diameter. into a spinning annulus of 1.5 cm diameter (48 mW/cm^2). Parts (B) and (C) are expanded regions of $NaNO_3$ Figure 3A UVRR.

band and the time dependence of the intensity of the upshifted NO_3^- $\nu1$ and $\nu3$ bands. Figure 4a shows that the NO_2^- intensity initially linearly increases and then levels off as the solid $NaNO_3$ surface layer converts to NO_2^-. In contrast, the appearance of the upshifted $\nu1$ and $\nu3$ bands show a short initial time delay, after which their intensities linearly increase (Figure 4b and c).

A distinctly different behavior is observed in Figure 5 that shows UVRR spectra which utilized an increase in flux and dose to illuminate a spinning solid $NaNO_3$ sample where the groove diameter was decreased to 2.5 mm (average flux = 465 mW/cm^2). The photochemical formation of the NO_2^- peaks is more extensive than in Figure 3, and the NO_2^- peak bandwidth increases at the higher dose values.

The NO_3^- $\nu1$ and $\nu3$ bands show distinctly different behaviors than those in Figure 3. The $\nu1$ band upshifts less and a lower frequency $\nu1$ band shoulder grows in at ~1050 cm^{-1}. The $\nu3$ band does *not* show the upshifted subband as observed at the lower dose flux conditions of Figure 3.

Figure 6 shows the dosage dependence of the NO_2^- $\nu1$ band intensity for this increased dose/flux condition. The intensity of the NO_2^- peak does not saturate at a dose of 0.01 mW sec μm^{-2}, but continues to increase up to the highest doses of 0.1 mW sec μm^{-2}.

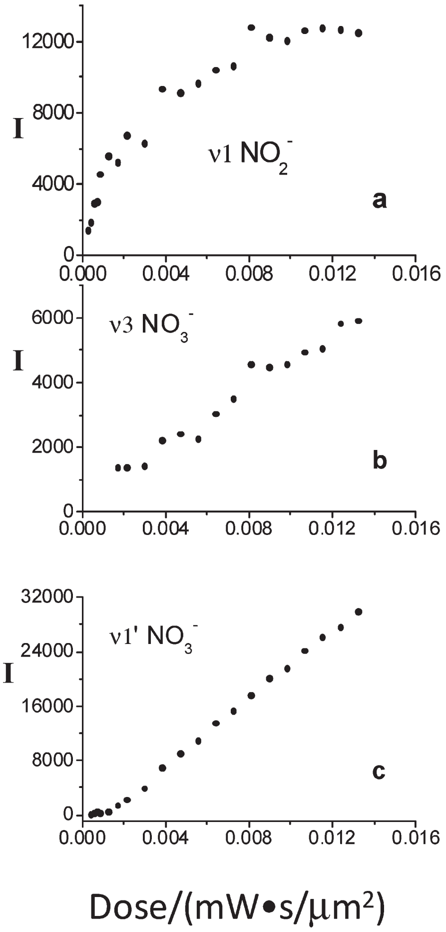

Figure 4. Dose dependence of 229 nm UVRR spectra of spinning solid $NaNO_3$ sample of a 1.5 cm annulus. Incident flux is 0.45 mW power into a 20 μm spot diameter (average flux = 48 mW/cm^2). (a) $\nu1$ NO_2^- band. Upshifted NO_3^- (b) $\nu3$ and (c) upshifted $\nu1$ bands.

Figure 7 shows the UVRR spectra of a *stationary* solid $NaNO_3$ sample at a constant, but higher fixed dose excitation 0.091 mW sec μm^{-2}), but where the incident power increases from 0.175 mW to 0.605 mW at the sample, while the illumination time decreases from 165 to 47 s.

Here we find that the observed NO_2^- $\nu1$ band intensity and the extent of photolysis are independent of flux but remain the same for constant dose. Each spectrum was measured at different regions of the sample. Each UVRR spectral measurement spanned the entire illumination period and the spectra were identically scaled.

The spectra are similar to one another indicating that the spectra are independent of the power flux and are sensitive mainly to the dose. Surprisingly, the extent of photolysis is similar to that observed in Figure 3, even though the dose is >1000-fold higher. Figure 8 shows that for this case the $\nu1$ band and $2\nu1$ band frequencies downshift in clear contradiction to the observed behaviors above.

The different behaviors observed for these different flux and dose conditions can be understood by examining the impact of illumination on the morphology of the solid $NaNO_3$ samples. Figure 9 shows the SEM and UVRR spectra of a solid $NaNO_3$ sample that was translated through the laser beam by using a translation stage while monitoring the sample UVRR. The sample was then sputter coated with Pd and its SEM measured.

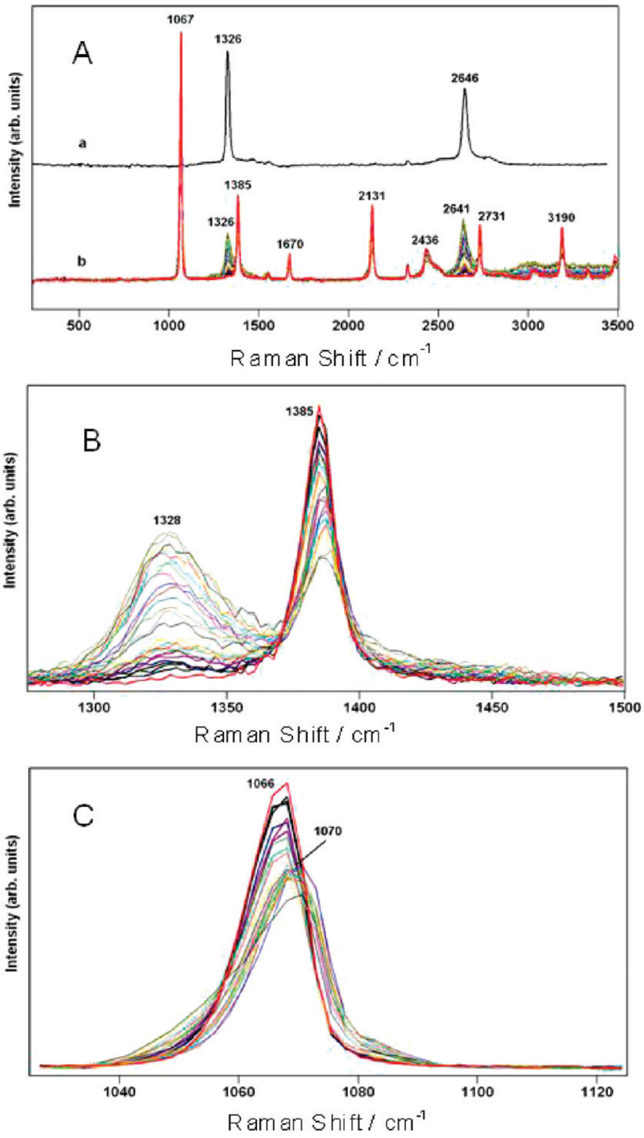

Figure 5. (A) Comparison of 229 nm UVRR spectra of (a) spinning sample of solid $NaNO_2$ to (b) spinning solid $NaNO_3$ sample as a function of illumination time. Incident flux is 0.7 mW power into a 20 μm spot diameter into a spinning annulus of 0.25 cm diameter (average flux = 461 mW/cm^2). (B) and (C) expanded regions of $NaNO_3$ UVRR.

The $NaNO_3$ sample was translated across the 20 μm diameter laser beam by hand rotating the translation stage micrometer at a rate of ~0.25 cm/min (with a time averaged flux of 54 W/cm^2). The Figure 9A SEM image shows the surface of a sample where the beam initially illuminates the bottom of the sample that was lowered vertically along the line L—K. The less evident part of the line around position L shows where the sample was translated at a rate of 0.25 cm/min during which the UVRR spectrum was collected. This translation resulted in a dose of ~5.4×10^{-4} mW·sec μm^{-2}, just below the lowest dose used in the Figure 4 data. The sample was stopped to measure the spectrum at point K in the sample, where it accumulated a dose of 8.5×10^{-2} mW·sec μm^{-2}. The Figure 9B and C SEM photographs show expanded views of the K and L regions. Further expanded views are shown in Figure 10.

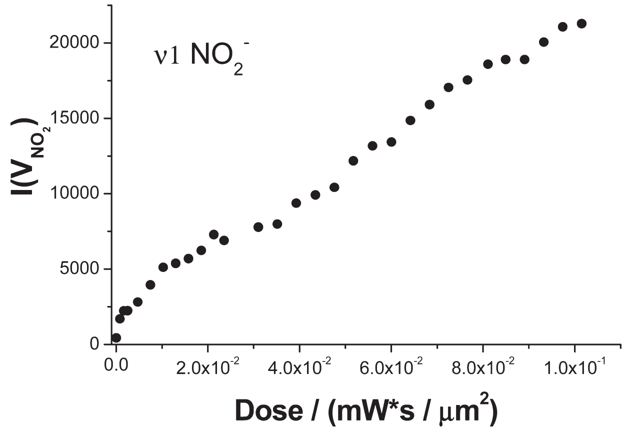

Figure 6. Dosage dependence of the NO_2^- $\nu 1$ band intensity for increased flux condition (average flux = 461 mW/cm^2). The NO_2^- peak intensity does not saturate at a dose of 0.01 mW sec μm^{-2}, but continues to increase up to the highest doses of 0.1 mW sec μm^{-2}.

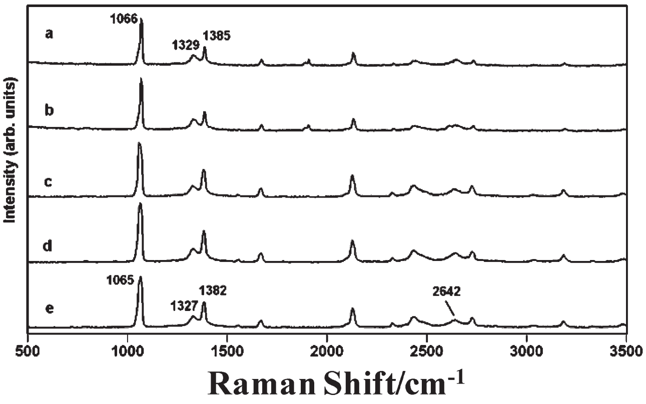

Figure 7. 229 nm UVRR of different regions of a stationary solid $NaNO_3$ sample following illumination at the following incident laser powers and illumination/acquisition times for a 229 nm laser beam focused to a 20 μm^2 laser spot at a constant dose of 0.091 mW sec μm^{-2}: (a) 0.605 mW, 47 s (190 W/cm^2); (b) 0.532 mW, 54 s (170 W/cm^2); (c) 0.373 mW, 77 s; (120 W/cm^2); (d) 0.252 mW, 114 s (80 W/cm^2); and (e) 0.175 mW, 165 s (60 W/cm^2).

Excitation with doses of 8.5×10^{-2} mW·sec μm^{-2} clearly disrupts the $NaNO_3$ solid sample. For the Figure 9 and 10 sample L regions we see surface eruptions as dots on the low dose edges of the illuminated lines. Closer to the middle of the line where the illumination intensity is a maximum these dots appear to coalesce to form crevice lines. The expanded SEM regions in Figure 10 show that in the center of the line, the higher dose intensities cause formation of connected regions of dots. In the case of the much higher doses in region K we see large craters and crevices where the surface material looks spongy.

The lowest dose measurements result in partial conversion of $NaNO_3$ to $NaNO_2 + O\cdot$. It is possible that the atomic oxygen formed quickly reacts to form O_2. Whatever the case, the increase in molecular species in the solid results in pressure induced stresses. For stress levels below the material failure threshold, the non-photolyzed $NaNO_3$ lattice sites will be compressed, resulting in an increased bond order and $\nu 1$ and $\nu 3$ vibration frequency increases, as observed in the Figure 3 UVRR spectra obtained at the low fluxes and doses that result in modest conversions to NO_2^-.

Higher flux and dose measurements result in failure of the material that relieves the stress. In this case, the upshifted $\nu 3$ band does not appear, while the $\nu 1$ band upshift decreases. Significant photochemical conversion to NO_2^- occurs which perturbs the NO_3^- frequency.

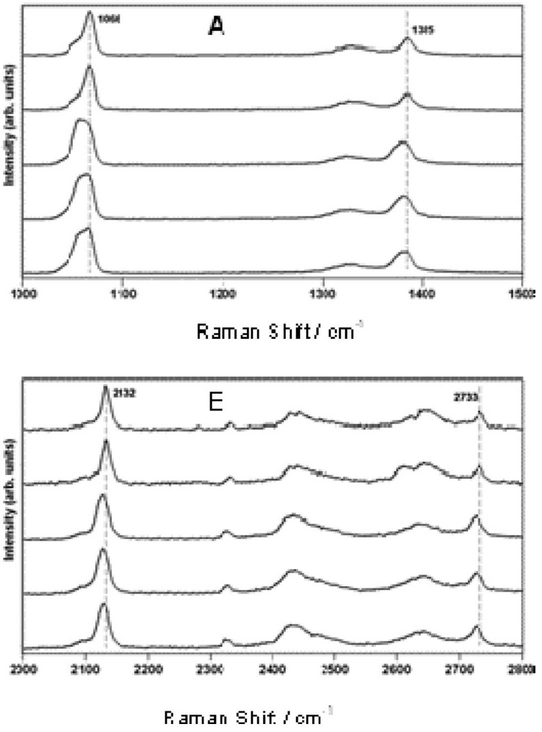

Figure 8. Expanded UVRR of the stationary solid $NaNO_3$ sample shown in Figure 7. The $\nu 1$ and $2\nu 1$ bands show spectral changes due to low frequency bandshifts.

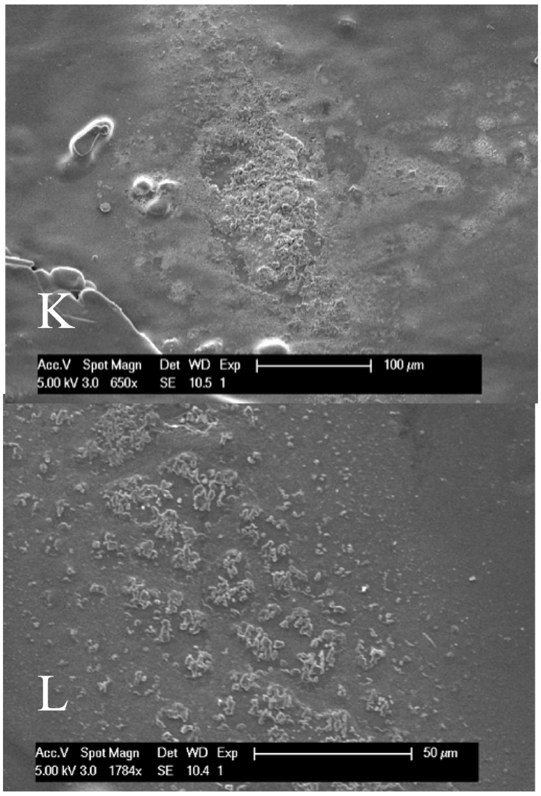

Figure 10. SEM expanded view of regions K and L of Figure 9.

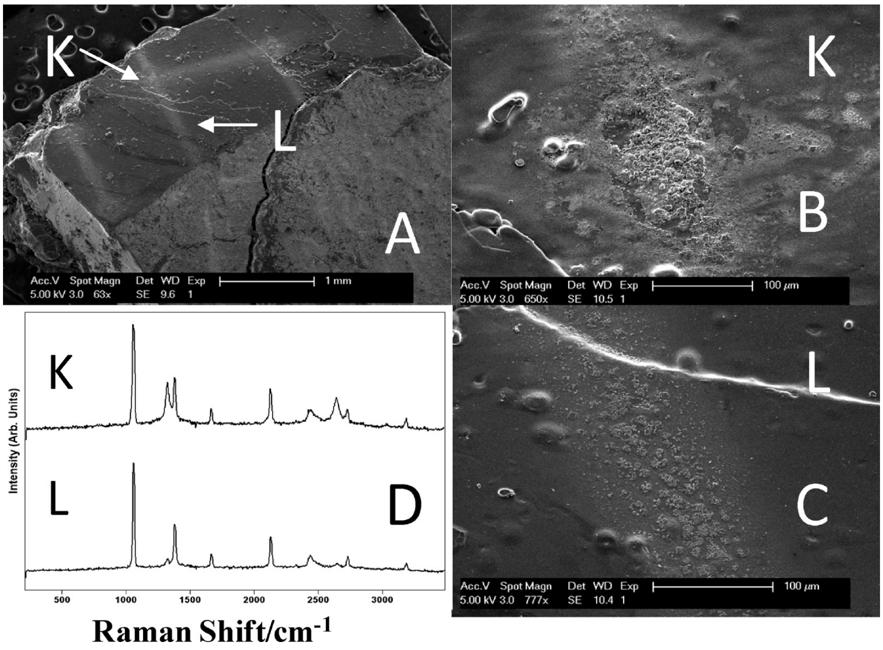

Figure 9. SEM and UVRR of illuminated solid $NaNO_3$ sample. The sample was illuminated with a 229 nm, 20 μm diameter ~0.5 mW beam (with an average flux of 6 W/cm^2). (A) Palladium coated $NaNO_3$ sample surface showing surface damage line along the L–K direction formed by translating the sample at a rate of 0.25 cm/min. Additional illumination lines are also evident. (B) Expanded SEM of K region where sample was stationary for a period of 1 min while measuring its UVRR. (C) Expanded SEM of L region where sample translated at a rate of ~0.25 cm/min through the beam while measuring the UVRR. (D) 229 nm UVRR of regions K showing extensive photochemistry, and region L with modest photochemistry due to translation of sample through the beam.

At the highest doses there is significant conversion to NO_2^- and the $NaNO_3^-$ lattice crumbles, forming a spongy looking material with craters that indicate that material is sloughed off. This is the reason that the sample surface layers never fully convert to NO_2^-; the NO_2^- product falls from the surface, exposing fresh $NaNO_3$. In this case the NO_3^- bands downshift as shown in Figure 8.

The increased pressure induced by the photolysis is concentrated at the sample surface and in a thin layer below where the photolysis is localized. The stressed $NaNO_3$ lies below layers of essentially pure $NaNO_2$. The outside surface $NaNO_3$ layers contain significant NO_2^- at the surface but the concentration of NO_2^- decreases with depth due to attenuation of the beam. The maximum pressure occurs in layers significantly photolyzed to NO_2^-. It is likely that the NO_2^- is not well ordered in the lattice and is brittle.

We can very roughly calculate the effective pressure if the photolysis simply results in conversion to only NO_2^- and O_2. Assuming full conversion to O_2 that expands into the total volume of the $NaNO_3$ the ideal gas law calculates a pressure of >300 atm assuming no excluded volume exists from the NO_2^- formed. The true pressure, thus, will be much higher and sufficient to cause the brittle NO_2^- overlayer to erupt.

Only in the lowest flux/dose measurements do we observe simple photolysis of the $NaNO_3$ sample. For this condition, we can use the rate of the NO_2^- $\nu1$ band intensity increase to calculate the photolysis quantum yield.

Solid State Photolysis Theory. It is easy to model the expected UVRR spectra that result from the photochemical conversion of $NaNO_3$ to $NaNO_2$ in the lattice if we assume photolysis subsequent to photon absorption at a constant quantum yield. Intrinsic to this calculation is the assumption that there is no diffusion of species within the ionic lattice and that there are no interactions between lattice sites. The photochemistry involved is: $NO_3^- + h\nu \rightarrow NO_2^-$.

The kinetics are: $(dN_B(r,t,\phi))/(dt) = -(dN_A(r,t,\phi))/(dt) = \phi I(r,t)N_A(r,t,\phi)\sigma_A = \phi I(r,t)\sigma_A\ (N_T - N_B(r,t,\phi))$, where $N_B(r,t,\phi)$ and $N_A(r,t,\phi)$ are the number density of NO_2^- and NO_3^- ions at position r in the lattice at time t. N_T is the original number density of NO_3^- in the unperturbed lattice. We assume that each lattice site is preserved during the photochemical conversion (vide infra). ϕ is the quantum yield for the photochemical conversion, $I(r,t)$, is the illumination intensity at position r in the crystal for normally incident light (photons/cm^2 s) at time t. $N_A(r,t,\phi)$ is the number density of NO_3^- in the lattice at position r and time t after beginning excitation. $\sigma_A = 2300\ \varepsilon/N_{av} = 1.3 \times 10^{-14}$ cm^2 is the 229 nm absorption cross section of the NO_3^- ion, which we assume is identical to the absorption cross section of NO_3^- in aqueous solution at 229 nm.[25]

N_{AV} is Avogadro's number. $N_T = 1000\ (\mathrm{cm}^3/\mathrm{L})\rho N_{AV}M_W^{-1}$ is the number density of NO_3^- in units of molc/L in the original lattice, where ρ is the density of $NaNO_3$ (2.26 g/cm^3),[34] and M_W is the molecular weight, 85 g/mol. The absorbances of NO_2^- and NO_3^- ions in water are essentially identical at 229 nm[25] and we use this fact to simplify our derivation.

$$\frac{dN_B(r,t,\phi)}{(N_T - N_B(r,t,\phi))} = \phi I(r,t)\sigma_A\ \boldsymbol{dt}$$

After integration we obtain an expression for the number of NO_2^- ions produced in the lattice:

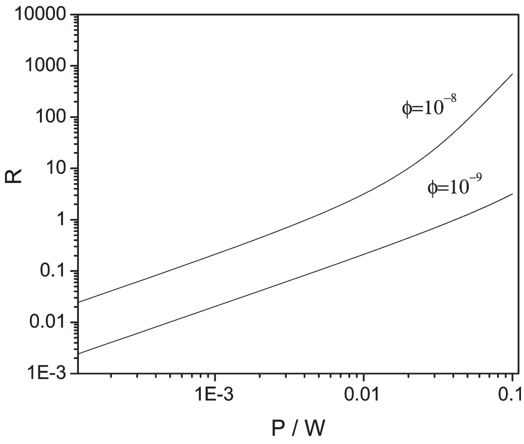

Figure 11. Dependence of R, the ratio of Raman intensities of NO_2^- and NO_3^- on the incident power on a solid sample of $NaNO_3$ showing the ratio for quantum yields of 10^{-9} and 10^{-8} for illumination time of 25 min, similar to that in Figure 3. The observed ratio of $R \approx 0.1$ for ~0.5 mW illumation for a 20 μm beam diameter for a 1.5 nm diameter illuminated sample annulus indicates that the quantum yield is ~10^{-8}.

$N_B(r,t) = N_T(1-e^{-\phi\sigma_A I_o t e^{-\gamma CT}})$, where $\gamma = 2.303\varepsilon$, where ε is the 229 nm molar extinction coefficient (3400 (mol/L)$^{-1}$cm^{-1}). The concentration C of the absorbing species remains identical at C = 26.59 mol/L and I_o is the CW laser intensity in photons/cm^2, where $I_o = P\lambda/Ahc$, where P is the laser power in W, λ is the wavelength (229 nm), A is the focused beam area on the sample where we ignore beam divergence over the short path length given the high absorbance.The h is Planck's constant and c is the speed of light.

We can calculate the relative Raman intensities for a backscattering measurement by accounting for self-absorption of the incident and Raman scattered light. Because the molar absorptivities of NO_2^- and NO_3^- are essentially identical at 229 nm[25] we can derive a relatively simple expression for the ratio, R of the NO_2^- to NO_3^- Raman intensities:

$$R = \frac{\sigma_B^R \int\int_0^{t_p} N_B(r,t,\phi)I_o(t)e^{-3\gamma Ct}\mathrm{d}r\mathrm{d}t}{\sigma_A^R \int\int_0^{t_p} [N_T - N_B(r,t,\phi)]I_o(t)e^{-3\gamma Ct}\mathrm{d}r\mathrm{d}t}$$

where $\sigma_B^R = 1.6 \times 10^{-25}$ cm^2 and $\sigma_A^R = 7.4 \times 10^{-26}$ cm^2 are the 229 nm Raman cross sections of NO_2^- and NO_3^-, respectively, estimated from spectra of these ions in aqueous solution.[4,25,35] The integration over r is from the surface ($r = 0$) to ∞, and over the measurement time interval, t_p.

We can determine the photochemical quantum yield from the power and time dependence of the relative NO_2^- to NO_3^- Raman intensities, R. Figure 11 shows the flux dependence of the value of R, the ratio of NO_2^- to NO_3^- for a solid $NaNO_3$ sample as in Figure 3 in a 1.5 cm diameter annular spinning cell, for a beam diameter of 20 μm we observe $R \approx 0.1$ after 25 min illumination. Figure 11 shows R for a 25 min illumination time and for quantum yields of $\varphi = 10^{-8}$ and $\varphi = 10^{-9}$. A quantum yield of $\varphi = 10^{-8}$ calculates an $R \approx 0.1$ value, close to that experimentally observed.

Although these quantum yields are very small, these ~0.5 mW excitation powers focused to small rotating cell annular excitation areas (~3×10^{-3} cm^2) result in large photon fluxes and

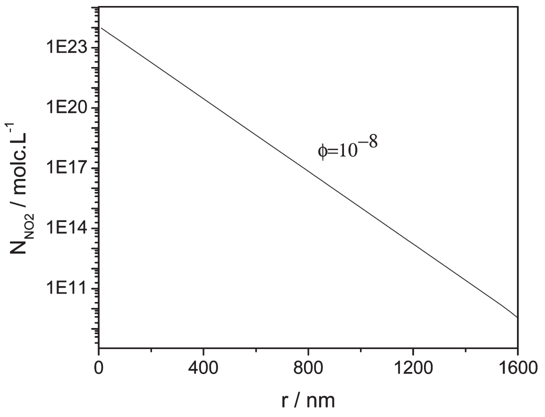

Figure 12. Dependence of NO_2^- number density (molc/L) as a function of depth into the sample for a 1 mW beam focused to a 20 μm diameter illuminating the solid sample for 50 s (1.15×10^{21} phot/cm^2). The original concentration of NO_3^- is 1.6×10^{25} molc/L.

significant photochemical doses giving rise to extensive conversion to NO_2^- in the surface layer.

The photochemistry of the solid sample proceeds from the surface into the bulk. The photochemical conversion depth is limited by the strong absorptions of NO_3^- and NO_2^-. Figure 12 shows that, as expected, the NO_2^- number density is a maximum at the sample surface and declines with distance r into the sample. For example, for 1 mW excitation power into a stationary 10^{-6} cm^2 area (1.15×10^{21} photon/cm^2) with $\phi = 10^{-8}$ we fully photolyze a surface layer ~20 nm thick within 25 min.

The ~million-fold quantum yield decrease for the solid compared to the solution state photochemistry is probably due to the lattice constraint in the solid that prevents formation of NO_2^- and O•. An Arrhenius kinetic estimate of the additional crystal activation barrier(s) over that in the liquid calculates a value of ~40 KJ/mol at room temperature.

The aqueous solution quantum yield is well-known to vary with pH indicating that further chemistry can impact the measured quantum yield.[17] However, the huge difference between the solid state and aqueous solution quantum yields is not likely to result from simple chemistry differences. It is possible that geminate recombination may be involved in the much lower apparent solid state quantum yield.

We should note that our measured solid $NaNO_3$ quantum yield is much lower than that measured by Doigan and Davis[36] who measured quantum yields of a variety of nitrate solids. We expect that their use of high power mercury arcs with their very high fluxes and short wavelengths resulted in much more aggressive photolysis conditions and possibly much higher temperatures.

Laser Induced Temperature Increase. We estimated the temperature increase induced by laser heating of the fully dense $NaNO_3$ solid samples using the expressions of Lax.[37] The laser heating is considered to result from a steady state temperature rise due to heating from laser beam absorption within a thin surface layer competing with heat diffusion out of the illuminated volume. A significant temperature increase due to laser heating could give rise to sample phase changes or induce chemical reactions[38] in addition to the room temperature photochemistry expected. Lax's treatment assumes high sample surface absorption where all of the incident light is absorbed within an infinitesimally thin layer, that is consistent with the $NaNO_3$/$NaNO_2$ solid sample absorption studied here.

The maximum temperature calculated by Lax is as follows:

$$T_{\max} = \frac{p}{2\pi K}\left\langle \frac{1}{r} \right\rangle$$

where

$$\left\langle \frac{1}{\gamma} \right\rangle \equiv \frac{1}{w}\left(\int_0^\infty f(R)\mathrm{d}R\right)\left(\int_0^\infty f(R)R\mathrm{d}R\right)^{-1} \cong \frac{1}{w}\pi^{1/2}$$

where P is the incident power (P = 1 mW), and K is the thermal conductivity. We estimate K = 30 mW/cm•K based upon values given for similar inorganic nitrates.[39] w is the beam diameter, and $\langle 1/r \rangle$ "is the mean inverse distance from a point on the surface at the beam center to the remaining points on the surface using a weight factor f(R)R proportional to the intensity incident (weighted by area) on the surface".[37]

We measured a beam full width at half-maximum of 20 μm. We, thus, calculated a maximum temperature rise of 5 °C for the incident power of 1 mW absorbed by an infinitesimally thin layer at the surface. Therefore, we conclude that laser heating does not contribute to any phase transitions or additional chemistry converting $NaNO_3$ to $NaNO_2$.

The situation, however, could significantly differ for the photochemically degraded sample which shows spongy surface structures that must have much smaller thermal conductivities. These damaged porous sample volumes may show additional thermally induced phenomena due to laser beam illumination.

■ CONCLUSIONS

Deep 229 nm excitation UVRR spectra of $NaNO_3$ in solution and the solid state show strong resonance enhancement of the NO_3^- fundamentals, overtones, and combination bands. These results indicate that the excited state is displaced relative to the ground state. If the excited state is not dissociative, then transfer to another excited state surface is required to generate the observed photochemistry. It appears unlikely that the vertically excited $\pi\pi^*$ state is dissociative given the previous theoretical UVRR excitation profile studies that find a bound $\pi\pi^*$ excited state somewhat expanded along the N–O bonds.[5,11,12]

We measure a quantum yield for a $NaNO_3$ neutral aqueous solution of 0.04. In contrast, in solid state $NaNO_3$ we measure a quantum yield of $\sim 10^{-8}$ that is dramatically decreased, probably due to the additional constraints by the lattice on the photochemical reaction coordinate(s). We estimate an increased activation barrier of ~40 kJ/mol. The resonant $\pi \rightarrow \pi^*$ transitions seem very similar for the aqueous solution and solid state nitrates in view of their very similar UVRR spectra.

Low photon flux/dose conditions result in pressurization of the lattice resulting in upshifts in the NO_3^- bands. Higher flux/dose conditions that significantly photolyze the sample surface result in high internal pressure that fracture the NO_2^- surface layer causing eruptions alleviating the pressure. Higher flux/dose measurements fracture the sample causing cratering and removal of the NO_3^- surface layers. In this case, although extensive photolysis occurs, the ratio of NO_2^-/NO_3^- UVRR intensities becomes constant as the laser beam penetrates the sample. The perturbed NO_3^- frequencies downshift due to the disorder caused by the photolysis.

The $NaNO_3$ UVRR spectral time dependence results from a competition between different dynamics occurring during the deep UV excitation. The photochemistry to NO_2^- is very fast yielding atomic oxygen. For low excitation fluxes, pressure builds up in the converting sample to shift the NO_3^- vibrational modes. The pressure buildup competes with effusion of the photochemically generated gases which include molecular oxygen. When the pressure exceeds the material failure threshold the sample erupts to release the gases. In this regime, the NO_3^- vibrational band frequencies shift due to perturbation of the environment due to exchange of adjacent NO_3^- lattice sites with NO_2^-.

The deep UVRR spectra measured are very intense and the UVRR spectra shows a time-dependent evolution that is characteristic of solid state $NaNO_3$. The bright UVRR of $NaNO_3$ in addition to its temporal spectra dependence makes it an excellent candidate for UVRR standoff detection. The laser flux/dose dependence of the UVRR can be used as a reliable confirming signature for the presence of this material.

■ AUTHOR INFORMATION

Corresponding Author

*E-mail: asher@pitt.edu.

■ ACKNOWLEDGMENT

We thank Kan Xiong for help preparing the figures. We acknowledge partial funding of this work by the West Virginia High Technology Consortium Foundation under Contract No. HSHQDC-09-C-00159 from the Department of Homeland Security Science and Technology Directorate.

■ REFERENCES

(1) Andrew, T. L.; Swager, T. M. *J. Am. Chem. Soc.* **2007**, *129*, 7254–7255.

(2) Guo, Y. Q.; Greenfield, M.; Bhattacharya, A.; Bernstein, E. R. *J. Chem. Phys.* **2007**, *127*, 154301.

(3) Moore, D. S. *Rev. Sci. Instrum.* **2004**, *75*, 2499–2512.

(4) Dudik, J. M.; Johnson, C. R.; Asher, S. A. *J. Chem. Phys.* **1985**, *82*, 1732–1740.

(5) Gaff, J. F.; Franzen, S.; Delley, B. *J. Phys. Chem. A* **2010**, *114*, 11681–11690.

(6) Heller, E. J. *Acc. Chem. Res.* **1981**, *14*, 368–375.

(7) Yang, Y.-Y.; Zink, J. I. *J. Am. Chem. Soc.* **1984**, *106*, 1500–1501.

(8) Shin, K.-S. K.; Zink, J. I. *Inorg. Chem.* **1989**, *28*, 4358–4366.

(9) Myers, A. B.; Mathies, R. A.; Tannor, D. J.; Heller, E. J. *J. Chem. Phys.* **1982**, *77*, 3857–3866.

(10) Shin, K.-S. K.; Clark, R. J. H.; Zink, J. I. *J. Am. Chem. Soc.* **1990**, *112*, 3754–3759.

(11) Waterland, M. R.; Myers Kelley, A. *J. Chem. Phys.* **2000**, *113*, 6760–6773.

(12) Waterland, M. R.; Stockwell, D.; Myers Kelley, A. *J. Chem. Phys.* **2001**, *114*, 6249–6258.

(13) Tuschel, D. D.; Mikhonin, A. V.; Lemoff, B. E.; Asher, S. A. *Appl. Spectrosc.* **2010**, *64*, 425–432.

(14) Daniels, M.; Meyers, R. V.; Belardo, E. V. *J. Phys. Chem.* **1968**, *72*, 389–399.

(15) Bayliss, N. S.; Bucat, R. B. *Aust. J. Chem.* **1975**, *28*, 1865–1878.

(16) Mark, G.; Korth, H.-G.; Schuchmann, H.-P.; v. Sonntag, C. *J. Photochem. Photobiol. A: Chem.* **1996**, *101*, 89–103.

(17) Mack, J.; Bolton, J. R. *J. Photochem. Photobiol. A: Chem.* **1999**, *128*, 1–13.

(18) Shuali, U.; Ottolenghi, M.; Rabani, J.; Yelin, Z. *J. Phys. Chem.* **1969**, *73*, 3445–3451.

(19) Fanning, J. C. *Coord. Chem. Rev.* **2000**, *199*, 159–179.

(20) Jankowski, J. J.; Kieber, D. J.; Mopper, K. *Photochem. Photobiol.* **1999**, *70*, 319–328.

(21) Thogersen, J.; Gadegaard, A.; Nielsen, J.; Jensen, S. K.; Petersen, C.; Keiding, S. R. *J. Phys. Chem. A* **2009**, *113*, 10488–10494.

(22) Boxe, C. S.; Colussi, A. J.; Hoffmann, M. R.; Perez, I. M.; Murphy, J. G.; Cohen, R. C. *J. Phys. Chem. A* **2006**, *110*, 3578–3583.

(23) Bykov, S.; Lednev, I.; Ianoul, A.; Mikhonin, A.; Munro, C.; Asher, S. A. *Appl. Spectrosc.* **2005**, *59*, 1541–1552.

(24) Asher, S. A.; Bormett, R. W.; Chen, X. G.; Lemmon, D. H.; Cho, N.; Peterson, P.; Arrigoni, M.; Spinelli, L.; Cannon, J. *Appl. Spectrosc.* **1993**, *47*, 628–633.

(25) Ianoul, A.; Coleman, T.; Asher, S. A. *Anal. Chem.* **2002**, *74*, 1458–1461.

(26) Paul, G. L.; Pryor, A. W. *Acta Crystallogr.* **1971**, *B27*, 2700–2702.

(27) Inorganic Crystal Structure Database, Fachinformationszentrum (FIZ) Karlsruhe, Germany, 2010.

(28) Downs, R. T.; Hall-Wallace, M. *Am. Mineral. Cryst. Struct. Database: Am. Mineral.* **2003**, *88*, 247–250.

(29) Narayanswamy, L. K. *Trans. Faraday Soc.* **1935**, *31*, 1411–1412.

(30) Irish, D. E.; Davis, A. R. *Can. J. Chem.* **1968**, *46*, 943–951.

(31) Brooker, M. H.; Irish, D. E.; Boyd, G. E. *J. Chem. Phys.* **1970**, *53*, 1083–1087.

(32) Brooker, M. H. *J. Phys. Chem. Solids* **1978**, *39*, 657–667.

(33) Ramesh, S. G.; Re, S.; Boisson, J.; Hynes, J. T. *J. Phys. Chem. A* **2010**, *114*, 1255–1269.

(34) *CRC Handbook of Chemistry and Physics*, 59th ed., pp B-167 (1978−1979).

(35) Asher, S. A.; Murtaugh, J. L. *Appl. Spectrosc.* **1988**, *42*, 83–90.

(36) Doigan, P.; Davis, T. W. *J. Phys. Chem.* **1952**, *56*, 764–766.

(37) Lax, M. *J. Appl. Phys.* **1977**, *48*, 3919–3924.

(38) Witke, K.; Klaffke, D.; Skopp, A.; Schreckenbach, J. P. *J. Raman Spectrosc.* **1998**, *29*, 411–415.

(39) *CRC Handbook of Chemistry and Physics*, 59th ed. pp. E-4 (1978−1979).